Geophys. J. Int. (2009) **176,** 740–752 doi: 10.1111/j.1365-246X.2008.04006.x

Advances in three-dimensional geoelectric forward solver techniques

M. Blome,[1] H. R. Maurer[1] and K. Schmidt[2]*

[1] *Institute of Geophysics, Federal Institute of Technology, Zürich, Switzerland. E-mail: mblome@aug.ig.erdw.ethz.ch*
[2] *Seminar for Applied Mathematics, Federal Institute of Technology, Zürich, Switzerland*

Accepted 2008 October 2. Received 2008 October 2; in original form 2008 April 18

SUMMARY

Modern geoelectrical data acquisition systems allow large amounts of data to be collected in a short time. Inversions of such data sets require powerful forward solvers for predicting the electrical potentials. State-of-the-art solvers are typically based on finite elements. Recent developments in numerical mathematics led to direct matrix solvers that allow the equation systems arising from such finite element problems to be solved very efficiently. They are particularly useful for 3-D geoelectrical problems, where many electrodes are involved. Although modern direct matrix solvers include optimized memory saving strategies, their application to realistic, large-scale 3-D problems is still somewhat limited. Therefore, we present two novel techniques that allow the number of gridpoints to be reduced considerably, while maintaining a high solution accuracy. In the areas surrounding an electrode array we attach infinite elements that continue the electrical potentials to infinity. This does not only reduce the number of gridpoints, but also avoids the artificial Dirichlet or mixed boundary conditions that are well known to be the cause of numerical inaccuracies. Our second development concerns the singularity removal in the presence of significant surface topography. We employ a fast multipole boundary element method for computing the singular potentials. This renders unnecessary mesh refinements near the electrodes, which results in substantial savings of gridpoints of up to more than 50 per cent. By means of extensive numerical tests we demonstrate that combined application of infinite elements and singularity removal allows the number of gridpoints to be reduced by a factor of ≈6–10 compared with traditional finite element methods. This will be key for applying finite elements and direct matrix solver techniques to realistic 3-D inversion problems.

Key words: Numerical solutions

1 INTRODUCTION

The introduction of multi-electrode data acquisition systems during the 1980s and 1990s has simplified significantly geoelectrical surveying, such that relatively large data sets can now be collected with a moderate field effort (e.g. Griffiths & Turnbull 1985; Stummer *et al.* 2002). This is certainly an important step towards routine application of 3-D surveys, but despite the ever increasing power of computers, realistic 3-D geoelectrical inversions remain challenging. In particular, the solution of the forward problem, that is, predicting electrical potentials using a particular conductivity model, can be a very time-consuming task.

During the past few decades much effort has been put into the development of numerical forward solvers. Among the methods used, the finite difference method (FDM) (Mufti 1976; Dey & Morrison 1979; Spitzer 1995; Zhao & Yedlin 1996; Wang *et al.* 2000), the finite element method (FEM) (Coggon 1971; Pridmore *et al.* 1981; Sasaki 1994; Bing & Greenhalgh 2001; Pain *et al.* 2002; Li & Spitzer 2002) are the most popular. Other methods proposed include the boundary element method (BEM) (Hvozdara & Kaikkonen 1998; Xu *et al.* 1998; Ma 2002) and the integral equation method (IEM) (Lee 1975; Dieter *et al.* 1969).

The FDM, first employed for geoelectrics by Mufti (1976) for 2-D and by Dey & Morrison (1979) for 3-D problems, has been the method of choice in the geoelectric community for a long time due to its easy and flexible implementation.

Unfortunately, finite difference calculations are generally restricted to structured, orthogonal grids that do not allow local mesh refinements. Only global refinements with respect to a single spatial coordinate can be implemented. This results in an unnecessarily large number of gridpoints. Furthermore, complicated topography can not be handled by orthogonal grids, although attempts have been made to circumvent this limitation (e.g. Loke & Barker 1996).

The FEM allows unstructured meshes to be used and is therefore much more flexible. In particular, complicated topographies can be implemented and the meshes can be almost arbitrarily coarsened or densified in regions where necessary. For example, Rücker *et al.*

*Now at: Hausdorff Center for Mathematics, University of Bonn, Bonn, Germany.

(2006) presented a 3-D geoelectric forward solver based on tetrahedral unstructured elements that clearly show the advantages of unstructured domain discretizations.

FDM and FEM are attractive options, when the subsurface conductivity distributions are highly heterogeneous. For less complicated subsurface structures, for example, a layered half-space with a few simply shaped inclusions, application of the BEM or IEM can be advantageous. For example, Ma (2002) provided BEM solutions for 3-D inhomogeneous bodies buried in a layered earth and Hvozdara & Kaikkonen (1998) used the BEM to calculate the response of a rectangular prism embedded in a homogeneous subsurface.

Due to its flexibility with regard to domain discretization and model complexity, the FEM is in our view currently the most appropriate method for 3-D geoelectrical inversion problems. Its implementation results in a system of equations of the form

$$\mathbf{Ax} = \mathbf{b}, \tag{1}$$

where matrix **A** represents the domain discretization and the conductivity model, vector **x** includes the unknown potentials or potential differences and vector **b** characterizes the geoelectrical sources. Matrix **A** is of the size $n \times n$, where n is the number of gridpoints in the finite element mesh. It can be very large (n is typically of the order 10^4–10^6 or even larger), but it is also extremely sparse.

Such systems of equations can be solved most efficiently with iterative solvers such as the preconditioned conjugate gradient method (Hestenes & Stiefel 1952; Spitzer 1995). During geoelectrical inversions the forward problem needs to be solved at least n_e times, where n_e is the number of electrodes employed. Typical 3-D surveys may include several hundreds of electrode positions. It is important to note that the finite element equations can easily be formulated such that only the right-hand side **b** of eq. (1) changes for the individual electrode positions. This motivates application of direct matrix solvers. Here, the matrix **A** is factorized in a lower and upper triangular matrix using LU decomposition. Once the factorization is performed, solutions for multiple right-hand side arguments **b** can be obtained swiftly by simple backsubstitutions. Despite this very attractive property, direct matrix solvers have been applied so far rarely for the solution of FEM problems. Main reasons for that include the expensive matrix factorization and, more importantly, the fact that the resulting triangular matrices are generally full, which is prohibitive in terms of memory requirements for typical FEM problems.

During the past few years significant new developments in sparse direct matrix solver techniques emerged (Schenk *et al.* 2003). Modern implementations are based on matrix reordering strategies that drastically reduce the memory consumption of the matrix factors. Still, for large 3-D forward problems the memory requirements of direct matrix solvers can be excessive. Fig. 1 illustrates advantages and limitations of direct matrix solvers. We employed the state-of-the-art 'PARDISO' solver (Schenk *et al.* 2001) for computing FEM solutions for different grid sizes. A nested dissection reordering strategy (Karypis & Kumar 1995) was chosen, which proved to be most efficient for our purposes. For comparison, we recomputed the solutions with an iterative preconditioned conjugate gradient solver.

For a single forward solution the direct and iterative solvers show comparable performance, but for the solution including multiple electrode positions, the direct matrix solver clearly outperforms the iterative algorithm (Fig. 1a).

The superiority of the direct matrix solver comes at the expense of memory usage. Despite the application of sophisticated matrix reordering strategies, its memory consumption is still about a factor of 10 higher compared with the iterative solver (Fig. 1b). Solutions of 3-D FEM problems including more than 10^6 nodes may thus require excessive amounts of memory.

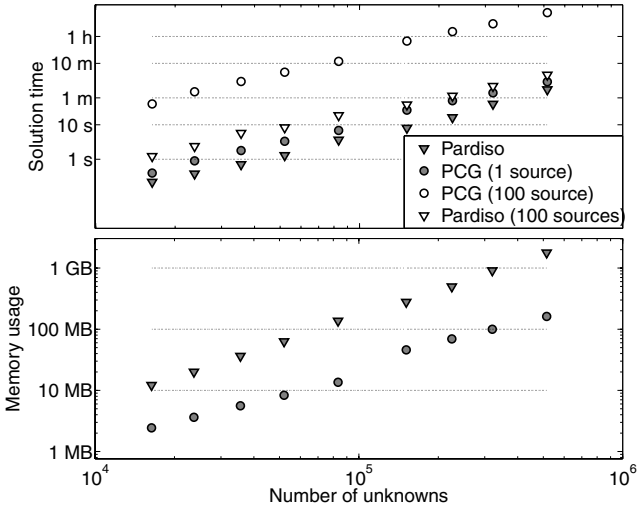

Figure 1. Comparison of the solution time and memory consumption of a preconditioned conjugate gradient solver (PCG, solver tolerance: 1×10^{-8}) and a direct matrix solver (Pardiso). For the tests the geoelectric problem has been solved with the FEM on a series of meshes.

In this paper we present two novel techniques that allow the number of gridpoints of FEM meshes to be reduced significantly. These developments thus allow very large 3-D geoelectrical forward problems to be solved with direct matrix solvers, which results in a considerable efficiency improvement of the corresponding inverse problem. The first technique is devoted to the reduction of nodes that are introduced to move the mesh boundaries (open boundaries within the subsurface) sufficiently far away from the model region of interest. This is achieved with the application of so-called infinite elements (Astley *et al.* 1998). Our second development concerns the mesh refinements near the electrode positions. Refinements are required to achieve a high solution accuracy near the singularities of the electrical potentials. Lowry *et al.* (1989) showed that the singularities at the electrodes can be removed by splitting the electrical potential in a singular part that can be computed analytically and a non-singular part that needs to be determined numerically. Unfortunately, analytical solutions for the singular potential exist only for special cases such as homogeneous or layered half-spaces without surface topography. We employ a fast multipole BEM technique (Hackbusch & Nowak 1989) that allows the singular potential for a homogeneous half-space with arbitrary topography to be computed efficiently.

In the first part of the paper we briefly review the fundamentals of the geoelectrical forward problem, the singularity removal technique and the finite element approximation to the governing partial differential equations. Then, we present the open boundary handling with infinite elements followed by a description of the fast multipole BEM technique that we employ for the singularity removal. The performance of these new developments is demonstrated with a series of numerical experiments. In particular, we show that the number of gridpoints can be reduced significantly without degrading the solution accuracy.

2 3-D GEOELECTRIC FORWARD MODELLING

2.1 Boundary value problem

The geoelectric forward problem is governed by the Poisson equation

$$\nabla \cdot (\sigma \nabla U) = -I_0 \delta(|\mathbf{r} - \mathbf{r}_s|) \qquad \text{in } \Omega \tag{2}$$

which results from the equation of continuity for a current strength I_0 injected at a source position r_s into a domain Ω with an arbitrary conductivity distribution σ. Here, we restrict the discussion to single current injection electrodes (pole–pole configuration). Commonly used 4-point electrode configurations can be obtained by superposition of pole–pole potentials.

The domain boundary Γ of Ω can be subdivided into a surface part Γ_s and a subsurface part Γ_g. Since no current can flow into the air, the Neumann boundary condition

$$\frac{\partial U}{\partial \mathbf{n}} = 0 \text{ on } \Gamma_s, \tag{3}$$

has to be applied on Γ_s($\mathbf{n}$ is the outward pointing normal vector on Γ_s). The ground boundary Γ_g is introduced only for numerical purposes to keep Ω finite. No exact boundary conditions along Γ_g exist. Mixed boundary conditions

$$\frac{\partial U}{\partial \mathbf{n}} + \beta U = 0 \text{ on } \Gamma_g \tag{4}$$

have proved to be a reasonable option for Γ_g, whereby the factor β has to be chosen to be $\beta = \mathbf{n} \cdot \mathbf{r}/|\mathbf{r}|^2$ for electrodes placed on Γ_s. Vector $\mathbf{r}$ represents the distance between the source electrode and the boundary Γ_g.

2.2 Singularity removal

The solutions of the geoelectric forward problem contain singularities at the source electrode positions due to the δ-function on the right-hand side of eq. (2). Near these singularities the electrical potential U varies rapidly. To obtain a numerically stable solution of eq. (2), a very fine spatial sampling around the electrodes is required, which is computationally inefficient. Lowry *et al.* (1989) presented an alternative approach in which the singularities are removed prior to the numerical solution. This is achieved by splitting the electrical potential U into a singular part U^s and a non-singular part U^n: In the absence of significant topography the singular potential can be expressed by an analytical homogeneous half-space solution

$$U_h^s = \frac{I_0}{2\pi\sigma_0} \frac{1}{|\mathbf{r} - \mathbf{r}_s|} \tag{5}$$

with σ_0 equal to the mean subsurface conductivity, as originally proposed by (Lowry *et al.* 1989), or, for a more accurate singularity removal, equal to the conductivity at the source electrode position (Zhao & Yedlin 1996).

Conceptually, more complex background conductivity models $\sigma_0(x, y, z)$, for which analytical or numerical solutions to eq. (2) exist, may be considered. For example, Li & Spitzer (2002) employed horizontally layered earth and vertical contact conductivity models for evaluating the singular potentials U^s.

Formally, the singularity removal is achieved by substituting $U = U^s + U^n$ on the left-hand side of eq. (2), and substituting

$$\nabla \cdot (\sigma_0 \nabla U^s) = -I_0 \delta(|\mathbf{r} - \mathbf{r}_s|) \tag{6}$$

on the right-hand side of eq. (2). Rearranging terms leads to a modified Poisson equation

$$\nabla \cdot [\sigma(\mathbf{r}) \nabla U^n] = -\nabla \cdot \{[\sigma(\mathbf{r}) - \sigma_0] \nabla U^s\}, \tag{7}$$

where the δ-function in the right-hand side has vanished. The problem is reduced to determining only the non-singular potential field that results from subsurface conductivities not equal to the background conductivity σ_0. Once the non-singular potential U^n is found, U^s is added to obtain the total electrical potential U.

When the singularity removal technique is applied, mixed type boundary conditions for U^n are not beneficial, because an approximate expression of the non-singular potential field is not known along the ground boundaries. Zhao & Yedlin (1996) suggest application of Dirichlet boundary conditions, that is, U^n should be forced to be zero along Γ_g.

2.3 Finite element equations

In the finite element method the domain Ω is subdivided in small subregions, which are referred to as finite elements. Within each element the unknown potential U^n (eq. 7) is approximated by a linear combination of so called shape functions α_k

$$U^n(x, y, z) = \sum_{k=1}^{p} \alpha_k(x, y, z) u_k^n, \tag{8}$$

where P denotes the number of nodes associated with a single element and u_k^n the unknown potential values at the nodes. Appropriate approximations for U^n should minimize the integral

$$\int_\Omega [\nabla \cdot [\sigma(\mathbf{r}) \nabla U^n] + \nabla \cdot \{[\sigma(\mathbf{r}) - \sigma_0] \nabla U^s\}\, \omega \mathrm{d}\Omega, \tag{9}$$

where ω is a weighting function. If the weighting functions are chosen to be equal to the shape functions α_k, the Galerkin solution is obtained (Zienkiewicz 1977). In order to employ linear shape functions, it is necessary to remove the second derivatives with respect to the potential U^n. This is achieved by applying Green's first identity to eq. (9), which results in the weak or variational form

$$\int_\Omega \sigma \nabla U^n \cdot \nabla \omega \mathrm{d}\Omega - \int_\Gamma \sigma \omega \frac{\partial U^n}{\partial \mathbf{n}} \mathrm{d}\Gamma = -\int_\Omega \nabla \cdot \{[\sigma(\mathbf{r}) - \sigma_0] \nabla U^s\}\, \omega \mathrm{d}\Omega. \tag{10}$$

Note that the corresponding expression for the total potential U (eq. 2) takes a similar form, but contains the δ-function under the volume integral on the right-hand side. After discretization by finite elements, eq. (10) leads to a linear system of equations. Since only the right-hand side of eq. (10) includes source electrode dependent terms, the system(s) of linear equations can be suitably solved with direct matrix solvers.

2.4 Domain discretization

We employ unstructured finite element meshes, which provide an enormous flexibility with regard to the mesh density inside Ω and the shape of the boundary Γ. In particular, this facilitates local mesh refinements in critical areas and allows straightforward implementation of arbitrary complicated surface topography. Fig. 2 illustrates our meshing procedure. At first the mesher is enforced to include nodes at the electrode positions [see label (1) in Fig. 2a]. The surface topography (e.g. measured via GPS in the field) is then discretized

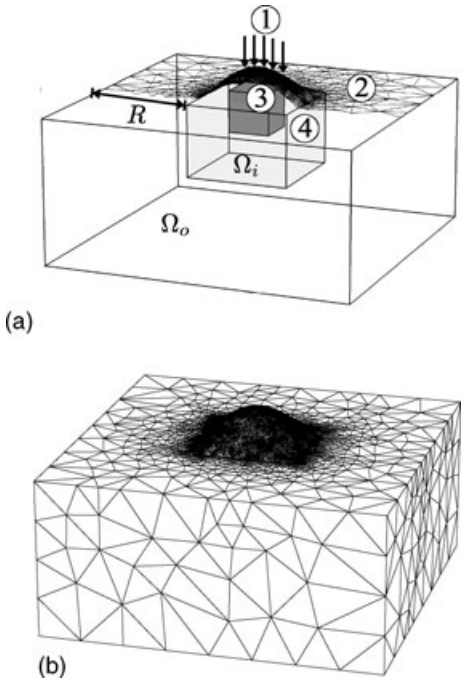

Figure 2. (a) Model description: 1: Electrode positions, 2: discretized surface topography, 3: optional internal boundaries, 4: inversion region (domain Ω_i). (b) The resulting finite element mesh.

by a triangular mesh (2). Internal boundaries, for example to represent boreholes, geological layers or conductivity model boundaries can optionally be defined (3). Inside the computational domain we choose a tetrahedron-based discretization. To ensure solution accuracy, a maximum size constraint for all tetrahedrons is specified in the region Ω_i below the electrode array (4). The inner region Ω_i is surrounded by an outer region Ω_o, whose extent is defined by the distance R. In our experience (and in accordance to Rücker *et al.* 2006) R should be approximately 5–10 times the size of the largest electrode spacing. Within Ω_o the mesh density decreases towards the model boundaries, whereby the growth rate of the finite elements is controlled by the maximum element aspect-ratio. The larger the ratio is, the more elongated the elements may be, hence the faster the element size can grow towards the boundary. Besides defining the element growth rate, the aspect-ratio constraint ensures reasonably well-shaped mesh elements. Badly shaped elements, that is, having a too large aspect-ratio, may degrade the solution accuracy (Wang *et al.* 2000). Fig. 2(b) shows an example of a suitably designed mesh.

Once the initial meshing is completed, local refinements can be applied (e.g. close to the source electrodes) by inserting additional nodes into the mesh. During the remeshing procedure the maximum aspect-ratio constraint is re-enforced, which automatically leads to a local refinement around the additional nodes. Optionally the finite element mesh can be converted to a second order finite element mesh. This is achieved by adding one additional node in the middle of each element edge. For our tetrahedron discretization this results in ten instead of four nodes per element. Quadratic shape functions are used to approximate the solution on second order finite elements (see eq. 8).

2.5 Open source FEM libraries

Our modelling algorithms are based on several public domain libraries that we modified for our purposes. In particular, we employed 'Triangle' (Shewchuk 1996) for discretizing the surface topography and the quality mesher 'Tetgen' (Si & Gaertner 2005) for performing the volume discretization. The matrix equation assembly routines rely on the finite element library 'Libmesh' (Kirk *et al.* 2006) and the resulting equations were solved with the direct matrix solver 'Pardiso' (Schenk *et al.* 2001). Furthermore, we used the FM-BEM classes in the numerical library 'Concepts' (Frauenfelder & Lage 2002) for the singularity removal.

3 OPEN BOUNDARY HANDLING VIA INFINITE ELEMENTS

The artificial ground boundaries Γ_g that appear in the finite element formulation to the Poisson equation are introduced only to keep the computational domain Ω finite. This inherently introduces errors in the numerical solution of eq. (2). To alleviate the problem, the outer domain Ω_o must be made very large, but this requires a significant number of additional elements and nodes, which would increase the computational costs unnecessarily.

Infinite elements, originally developed in the field of acoustic radiation (Bettes 1987), provide a cost-effective and elegant alternative to deal with open boundary problems. Instead of truncating the domain at a certain distance away from the electrode array, the outer domain is modelled by infinite elements. We employ the so-called 'Astley–Leys' elements, originally developed by Astley *et al.* (1998) and later-on refined for an improved conditioning of the resulting linear system of equations by Dreyer & Estorff (2003).

The infinite elements are attached to the subsurface boundary Γ_g as shown in Fig. 3(a). In contrast to the traditional approach using mixed-type or Dirichlet boundary conditions, the extent of Ω_o can be much smaller, that is, the distance R in Fig. 2(a) needs to be equal to only about half the largest electrodes spacing (compared to a factor of 5–10 for the traditional approach). A single pole inside the FE mesh is chosen at point $\mathbf{r}_p$ for all infinite elements to define the infinite elements radial directions (Fig. 3a). We choose $\mathbf{r}_p$ in the horizontal directions to coincide with the geometric mean of all source electrode positions because the potential fields decrease radially outwards from the source electrodes. The vertical location of $\mathbf{r}_p$ is given by the zero level of the topography to assure a well-shaped continuation of the finite element domain by the infinite elements.

The prismatic-shaped infinite elements are made-up of nine nodes. The first three nodes coincide with the triangular faces on the boundary Γ_g [nodes 1,2 and 3 located at $\mathbf{r}_1^i$ $(i = 1, \ldots, 3)$] and the outer three nodes (4, 5 and 6) are located at positions $\mathbf{r}_2^i = \mathbf{r}_1^i + (\mathbf{r}_1^i - \mathbf{r}_p)$ as shown in Fig. 3(a). The last three nodes $\mathbf{r}_3^i$ are located at an infinite distance away from $\mathbf{r}_p$ in direction of $\mathbf{n}^i = \mathbf{r}_2^i - \mathbf{r}_1^i$ and are thus not displayed in Fig. 3(a). The infinite extend of the infinite elements in the radial direction allows the potential field to be approximated up to infinity instead of truncating it at the domain boundaries Γ_g.

A coordinate transformation from the global (x, y, z)-coordinate system to the local (ξ, η, ν)-coordinate system is used to perform the integration necessary to set up the FEM equations:

$$\mathbf{r}^i(\nu) = \frac{-2\nu}{1-\nu}\mathbf{r}_1^i + \frac{1+\nu}{1-\nu}\mathbf{r}_2^i. \tag{11}$$

As shown in Fig. 3, this transformation maps the nodes located at $\mathbf{r}^i = \{\mathbf{r}_1^i, \mathbf{r}_2^i, \infty \cdot \mathbf{n}^i\}$ to the coordinates $\nu = \{-1, 0, 1\}$ in the local (ξ, η, ν)-coordinate system, where the integration can be carried out efficiently with standard Gaussian quadrature rules.

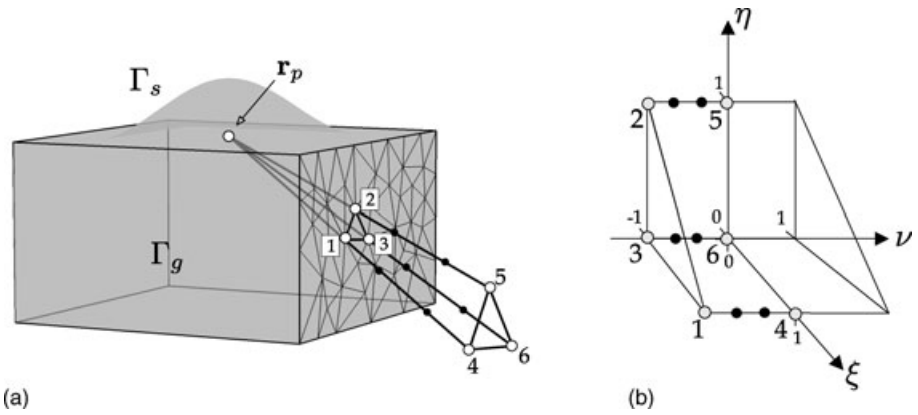

Figure 3. (a) A sample infinite element attached at the ground boundary Γ_g of a FE mesh. The infinite elements are constructed by choosing a common pole that defines their radial direction. The geometry of the infinite elements is defined by projecting rays from the pole through the triangular boundary faces outwards. The outermost three nodes that lie at infinity, are not displayed in this figure. (b) In local coordinates the infinite elements are mapped to a finite extent, where the numerical integration is carried out.

The infinite elements are endowed with standard linear or second order finite element shape functions S_i in the ξ, η-plane and with special shape functions in the radial direction (ν) that are based on Jacobi polynomials $P_i^{(2,0)}$. The order of the Jacobi polynomials can be chosen between 3 and 14, where higher radial orders will give rise to additional degrees of freedoms (indicated by the small black dots in Fig. 3). In our experience a radial order of 5 yields sufficiently accurate results. Finally, the approximation of the potential U inside the infinite elements is given by:

$$U = \sum_i U_i \widetilde{\phi}_i \text{ with } \widetilde{\phi}_i = 1/2 S_i(\xi, \eta)(1-\nu) P_i^{(2,0)}(\nu) \tag{12}$$

Modified test functions are chosen to improve the conditioning of the resulting equations (Dreyer & Estorff 2003). The resulting element matrices are slightly different to the ones obtained for conventional finite elements (compare to eq. 10):

$$\mathbf{A}^n_{i,j} = \int_{\Omega_n} \sigma_n \nabla \widetilde{\phi}_i \cdot (\widetilde{\phi}_j \nabla D_j + D_j \nabla \widetilde{\phi}_j) \mathrm{d}\Omega_n. \tag{13}$$

Here $\widetilde{\phi}_i$ are the infinite elements shape functions as defined in eq. (12) and $D(\nu) = [(1-\nu)/2]^2$ are additional radial weights.

In contrast to conventional finite element matrices, the matrices $\mathbf{A}^n$ are asymmetric (due to the radial weight functions D). Therefore, infinite elements lead to slightly asymmetric system matrices. Consequently, we choose either a preconditioned 'quadratic minimum residual' iterative solver or the LU direct solver implemented in 'Pardiso' to solve the resulting system of equations.

Performance of infinite elements is demonstrated in Fig. 4, which shows the non-singular potential field caused by a cuboid-shaped anomaly. The singularity removal technique leads to sources inside the conductivity anomaly that can physically be interpreted as charges accumulating along the conductivity contrasts (Mendonca 2003). These charges create a potential field with a dipolar character. As shown in Fig. 4, the dipolar field is continued properly into the area of the infinite elements. If Dirichlet boundary conditions would have been applied, the potential lines at Γ_g would have been forced to be parallel to the domain boundaries. This unphysical constraint would certainly have led to errors in the potential field computations.

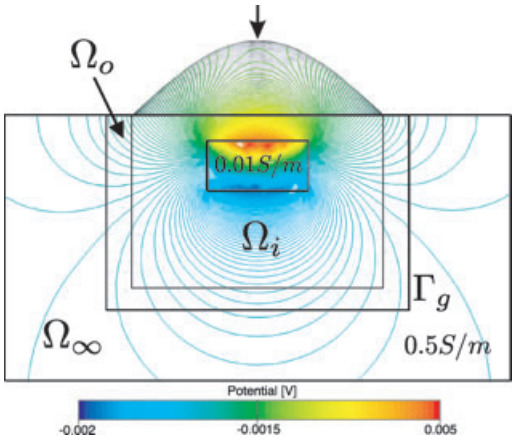

Figure 4. Non-singular potential field for a prismatic-shaped anomaly embedded in a homogeneous background. The potential field is accurately continued beyond the boundaries of the finite element mesh (region Ω_o).

4 SINGULAR POTENTIAL EVALUATION USING A FAST MULTIPOLE BEM

As discussed in Section 2.2, the singularity removal technique allows computation of electrical potentials without excessive grid refinements around the electrodes, but it requires the singular potential to be calculated separately. Unfortunately, no analytical solution exists for homogeneous half-spaces with significant surface topography, but the principal features of the BEM (Xu *et al.* 1998; Ma 2002) make this method very suitable for this purpose. In the following, we restrict ourselves to surface electrodes, but the same formulation with minor modifications is applicable to buried electrodes.

4.1 Boundary integral equation

When solving the singular potentials with the BEM, the Poisson equation

$$\begin{cases} \sigma_0 \nabla^2 U^s = -I_0 \delta(\mathbf{r} - \mathbf{r}_0) & \text{in } \Omega \\ \partial U^s / \partial \mathbf{n} = 0 & \text{on } \Gamma_s \\ U^s = 0 & \text{on } \Gamma_g \end{cases} \tag{14}$$

needs to be transformed into a Laplace equation with modified boundary conditions. Note that the choice of the ground boundary conditions in eq. (14) (Dirichlet type in this case) is arbitrary, because the BEM allows the artificial ground boundaries to be eliminated anyway. The transformation to the Laplace equation is achieved by splitting the singular potential solution U^s into a homogeneous part U^s_h and an inhomogeneous part U^s_i:

$$U^s = U^s_i + U^s_h \text{ with } U^s_i(\mathbf{r}) = \frac{I_0}{2\pi\sigma_0}\frac{1}{|\mathbf{r}-\mathbf{r}_0|} \tag{15}$$

and solving only for the homogeneous part of the solution under modified boundary conditions

$$\begin{cases} \sigma_0\nabla^2 U^s_h = 0 & \text{in } \Omega \\ \partial U^s_h/\partial\mathbf{n} = -\partial U^s_i/\partial\mathbf{n} & \text{on } \Gamma_s \\ U^s_h = -U^s_i & \text{on } \Gamma_g. \end{cases} \tag{16}$$

After the solution U^s_h has been found with the BEM, the inhomogeneous solution is added to yield the total singular potential U^s. Due to the linearity of eq. (16) with respect to σ_0, U^s can be estimated for an arbitrary value of σ_0 and later scaled to meet the true conductivity at the source electrode. In this way, the singular potentials need to be estimated only once prior to an inversion process. In the following discussion we assume $\sigma_0 = 1$.

As for the finite element equations we use Galerkin's criterion to derive the boundary integral equation corresponding to eq. (16):

$$\int_\Omega \nabla^2 U^s_h(\mathbf{r}) G(\mathbf{r},\mathbf{r}')\,\mathrm{d}\Omega = 0. \tag{17}$$

Here $G(\mathbf{r},\mathbf{r}')$ denotes the Green's function to the Laplace operator ∇^2. Applying Green's first identity twice yields the boundary integral equation:

$$\underbrace{\int_\Omega U^s_h(\mathbf{r})\nabla^2 G(\mathbf{r},\mathbf{r}')\,\mathrm{d}\Omega}_{k\,U^s_h(\mathbf{r}')} + \int_\Gamma U^s_h(\mathbf{r})\frac{\partial G(\mathbf{r},\mathbf{r}')}{\partial\mathbf{n}}\,\mathrm{d}S_\mathbf{r}$$
$$= \int_\Gamma \frac{\partial U^s_h(\mathbf{r})}{\partial\mathbf{n}} G(\mathbf{r},\mathbf{r}')\,\mathrm{d}S_\mathbf{r}, \quad \begin{cases} k = 1 & \text{for } \mathbf{r}' \text{ in } \Omega \\ k = 1/2 & \text{for } \mathbf{r}' \text{ on } \Gamma. \end{cases} \tag{18}$$

In contrast to the FEM approach, where local basis functions are chosen as the weighting function, full space Green's functions $G(\mathbf{r},\mathbf{r}')$ are employed in the BEM. Usually homogeneous subsurface solutions are used, but in general Green's functions for arbitrary background conductivity models may be employed, though expressions for these functions can be hard to find or may not exist at all. Ma (2002), for instance, demonstrated the use of layered background conductivity models in BEM calculations. The Green's functions are fundamental solutions to the Laplace operator, therefore the volume integral in eq. (18) reduces to simple function evaluations. Only boundary integrals remain to be evaluated and consequently only the boundary of the domain Ω needs to be discretized. The dimensionality of the problem is reduced from 3-D to 2-D, resulting in a substantial reduction of the number of unknowns in the equations to be solved. For evaluation points $\mathbf{r}'$ on Γ eq. (18) leads to an integral equation that relates U^s_h on Γ to integral expressions over Γ and therefore can be used to solve for the singular potentials along the boundary of the domain. Subsequently, by choosing evaluation points $\mathbf{r}'$ in Ω, eq. (18) can be used to evaluate the singular potentials inside the domain. Mathematical analysis (e.g. Sauter & Schwab 2004) shows that in the first case eq. (18) is valid for $k = 1/2$ whereas in the latter case $k = 1$ results.

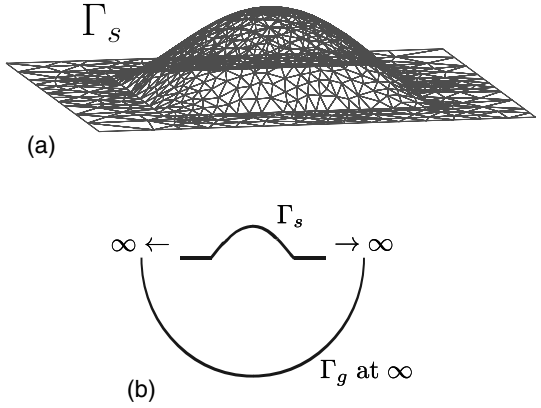

Figure 5. (a) A typical surface mesh used in the BEM (only the inner, that is, topographic part is shown here). (b) By moving the ground boundaries to ∞, only the inner part of the surface Γ_s needs to be discretized.

The absence of volume integrals in the BEM allows for a very natural handling of the unbounded domain that occurs during the computation of the singular potentials. Fig. 5(b) depicts a sketch of the integration principle. Instead of truncating the domain at a certain distance away from the source electrodes the ground boundaries Γ_g are moved to infinity. As U^s_i, and therefore, U^s_h approaches 0 at an infinite distance away from the source electrode, the boundary integrals along Γ_g vanish. Along Γ_s the integration can be truncated after a certain distance away from the source ($\approx$5–10 times the largest electrode distance) when $\partial U^s_h/\partial\mathbf{n} = -\partial U^s_i/\partial\mathbf{n} \approx 0$ and thus only an inner part of Γ_s needs to be discretized. Fig. 5(a) shows an example triangular mesh used for the BEM (for clarity, the outer part of the mesh is not shown).

To obtain accuracy and stability of the solution we employ a weak formulation of the boundary integral eq. (18):

$$\frac{1}{2}\int_{\Gamma_s} U^s_h(\mathbf{r}')\phi(\mathbf{r}')\,\mathrm{d}S_{\mathbf{r}'} + \int_{\Gamma_s}\int_{\Gamma_s} U^s_h(\mathbf{r})\frac{\partial G(\mathbf{r},\mathbf{r}')}{\partial\mathbf{n}}\phi(\mathbf{r}')\,\mathrm{d}S_\mathbf{r}\,\mathrm{d}S_{\mathbf{r}'}$$
$$= \int_{\Gamma_s}\int_{\Gamma_s} \frac{\partial U^s_h(\mathbf{r}')}{\partial\mathbf{n}} G(\mathbf{r},\mathbf{r}')\phi(\mathbf{r}')\,\mathrm{d}S_\mathbf{r}\,\mathrm{d}S_{\mathbf{r}'}. \tag{19}$$

After discretization by unstructured triangular elements with linear shape functions ϕ_i eq. (19) leads to a linear system of equations

$$\mathbf{A}\mathbf{u}^s_h = \mathbf{B}\mathbf{q} \tag{20}$$

with the matrix entries given by

$$\mathbf{A}_{ij} = 1/2\int_{\Gamma_s}\phi_i(\mathbf{r})\phi_j(\mathbf{r}')\,\mathrm{d}S_{\mathbf{r}'} + \int_{\Gamma_s}\int_{\Gamma_s}\phi_i(\mathbf{r})\frac{\partial G(\mathbf{r},\mathbf{r}')}{\partial\mathbf{n}}\phi_j(\mathbf{r}')\,\mathrm{d}S_\mathbf{r}\,\mathrm{d}S_{\mathbf{r}'} \tag{21}$$

$$\mathbf{B}_{ij} = \int_{\Gamma_s}\int_{\Gamma_s}\phi_i(\mathbf{r})G(\mathbf{r},\mathbf{r}')\phi_j(\mathbf{r}')\,\mathrm{d}_\mathbf{r}\,\mathrm{d}S_{\mathbf{r}'}, \tag{22}$$

and the Neumann boundary condition values

$$\mathbf{q}_i = \partial U^s_{h,i}/\partial\mathbf{n}_i. \tag{23}$$

Eq. (20) yields the unknown potential values $\mathbf{u}^s_h$ on the nodes of the surface mesh. Subsequently, eq. (18) needs to be re-evaluated in a second step to obtain the potential solution inside the volume (i.e. at all nodes of the corresponding FE mesh).

4.2 The fast multipole BEM

The BEM matrices **A** and **B** in eqs (21) and (22) are fully populated due to the coupling of the Green's function $G(\mathbf{r}, \mathbf{r}')$. Consequently, the computational costs, memory consumption and solution time, scale as $\sim \mathcal{O}(N^2)$ for the BEM while they scale as $\sim \mathcal{O}(M)$ for the FEM, for which system matrices are usually extremely sparse (here N and M denote the number of unknowns in the BEM, respectively the FEM equations). This imposes a serious limitation on the applicability of the BEM, because especially the unfavorable memory consumption may easily render the BEM inefficient compared to the FEM.

To account for this major drawback of the standard BEM, fast multipole boundary element methods (FM–BEM) where introduced (Hackbusch & Nowak 1989). These methods employ the fast multipole method originally developed by (Greengard & Rokhlin 1987) by expanding the Green's function $G(\mathbf{r}, \mathbf{r}')$ in the farfield by a function series such that the variables **r** and **r**′ are separated. With this kernel expansion the matrix assembly and the solution times are considerably reduced by combining the effects of Green's function evaluation points in the farfield to so-called multipole moments. In the nearfield, that is, where **r** and **r**′ are close-by, standard Green's function evaluations are used. Effectively, this scheme leads to an approximation of the fully populated BEM matrix by a sparse nearfield matrix and a sum of low-rank farfield approximation matrices. The FM–BEM employs a multilevel scheme to exploit the use of multipole moments as efficiently as possible. The computational costs for matrix vector products needed when solving the resulting system of equations with iterative solvers is reduced from $\sim \mathcal{O}(N^2)$ to $\sim \mathcal{O}[N \log^{\alpha}(N)]$. We employ a variant of the FM–BEM called 'Panel Clustering Method' implemented by (Lage 1995) to solve for the singular potentials efficiently. Details about the method used can be found in Appendix A.

5 NUMERICAL TESTS

5.1 Test models

Numerical simulations were carried out for 3 different conductivity models: (i) a homogeneous conductivity model, (ii) a model including a single prismatic anomaly within the homogeneous host rock (Fig. 6a) and (iii) an embedded stack of two layers (Fig. 6b). All three models included a mound-shaped topography on which 50 electrodes were placed. For each model we performed calculations on a series of 18 meshes with increasing numbers of unknowns. The mesh size was increased by moving the ground boundaries outwards and at the same time increasing the mesh density in the inner part Ω_i (Fig. 6c). In the outer part of the mesh Ω_o, the increasing mesh size towards the boundaries was controlled by a maximum aspect ratio constraint as described in Section 2.4. The meshes were chosen such that the numbers of unknowns were roughly equidistant on a logarithmic scale to cover a wide range of problem sizes. Meshing was performed such that all mesh elements lied entirely within a region of constant conductivity to avoid model discretization errors.

5.2 Potential field calculations

Computations were carried out for each conductivity model, electrode position and mesh size. Moreover, all computations were performed with both, first and second order finite elements. The entire suite of these simulations were repeated using (i) standard FEM with mixed-boundary conditions, (ii) infinite elements, (iii) numerical singularity removal using FM–BEM and (iv) combined application of infinite elements and numerical singularity removal. Computations with infinite elements did not require the outer space Ω_o to be meshed ($R = 0.2$ was chosen such that its boundaries were sufficiently far away from the conductivity anomalies and the outermost electrodes). Since the quality mesher employed created already a very efficient grid in Ω_o, this saved only 5–10 per cent of the unknowns, but it was expected that the properties of the infinite elements would generally lead to improved accuracy. Computations involving numerical singularity removal did not require mesh refinements near the electrodes, which led to a ≈10–65 per cent reduction of the unknowns. Finally, combined application of infinite elements and numerical singularity removal was expected to provide the best ratio of accuracy and number of unknowns.

Unfortunately, no analytical solution exists for estimating the accuracy of the different simulations. Therefore, we compared our results with reference solutions that were obtained by the finite element forward solver described in (Rücker *et al.* 2006). These reference solutions were calculated on extremely dense meshes equipped with second-order shape functions (each including more than 1 million unknowns). Mixed boundary conditions were applied and a preconditioned conjugate gradient solver with a solver tolerance of 1×10^{-9} was used.

Initial inspection of the simulation results revealed that the solution accuracy was comparable for all electrode positions. For the sake of simplicity, we therefore, restricted our further analysis to the results obtained with an injection electrode at the top of the mound shaped topography (vertical arrows in Fig. 6). Simulation results are summarized in Fig. 7. It displays the median errors of all gridpoints relative to the corresponding reference solutions as a function of

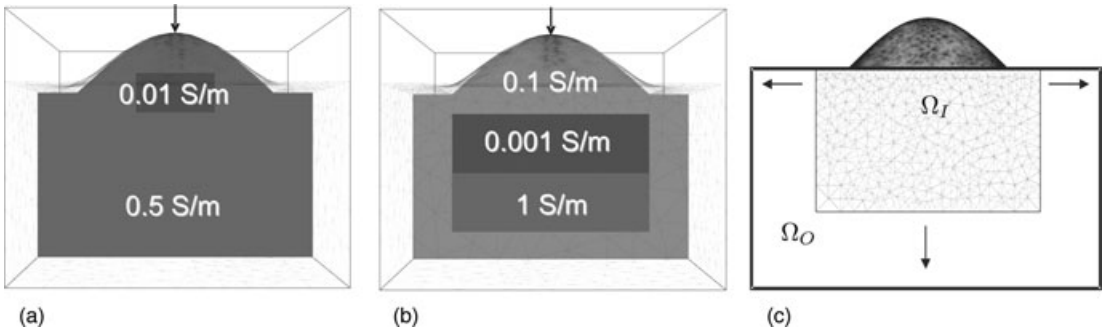

Figure 6. (a) Cuboid model (b) Layered block model (c) The mesh size is increased by moving the subsurface boundaries outwards and increasing the mesh density in the inner part Ω_i.

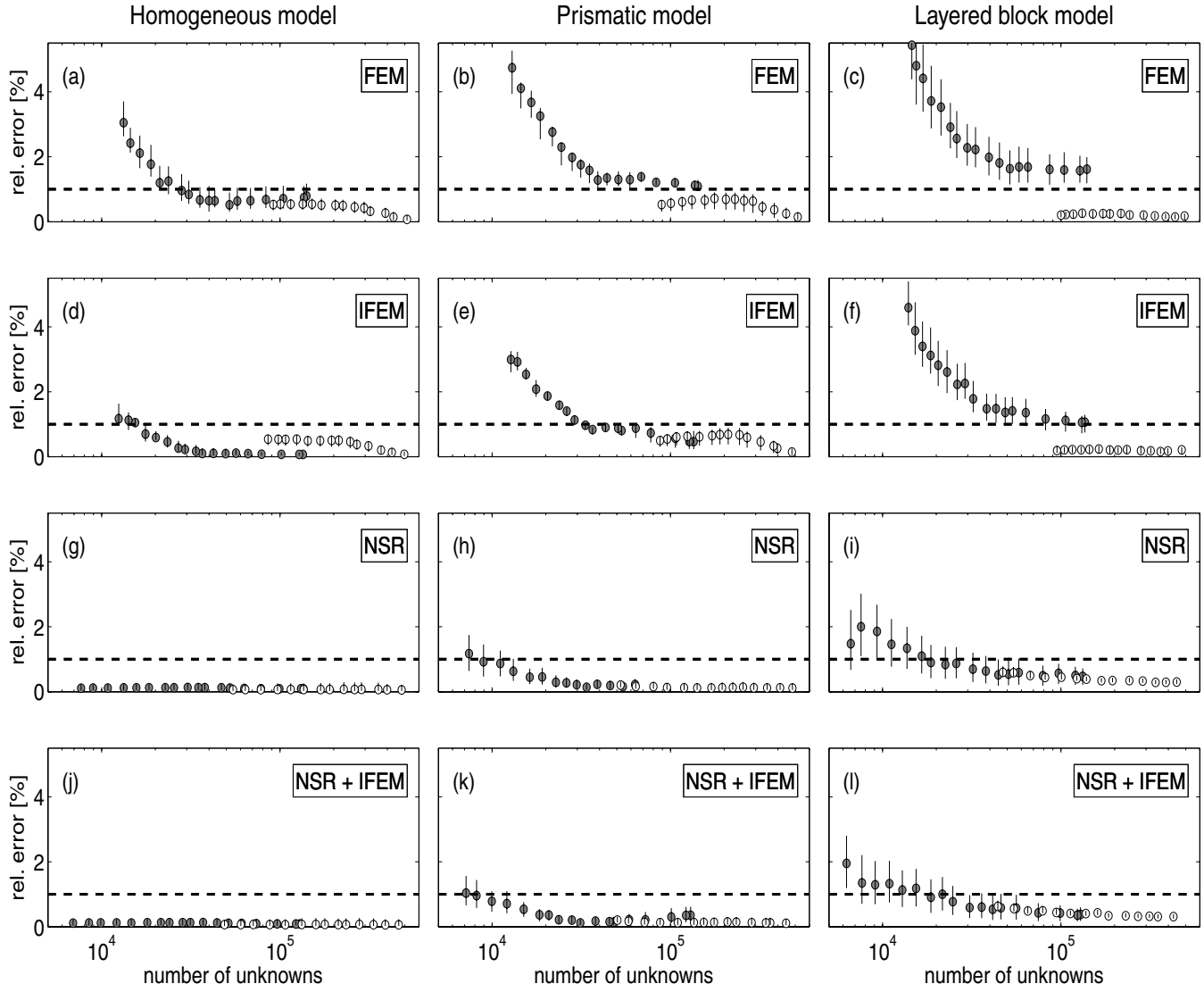

Figure 7. Numerical results of the forward solver for three different conductivity models and the new forward solver techniques. Each subplot shows the median relative solution errors (in per cent) together with the 25 and 75 percentiles (error bars) estimated for a series of meshes with increasing number of unknowns. Results are displayed for first order (filled dots) and second order finite element approximations (blank dots). Labels: FEM: *SD* FEM calculations, IFEM: *SD* FEM with infinite elements, NSR: Numerical singularity removal.

the mesh sizes. Additionally, the 25 and 75 percentiles (error bars) are shown for a robust estimate of the error variability. We have chosen a target median relative error of 1 per cent as an acceptable solution. This target value is marked with a solid horizontal line in the panels of Fig. 7.

Using the standard FEM with mixed boundary condition and the coarsest mesh (with the least number of unknowns) provided solution accuracies of about 4 per cent (Figs 7a–c), but it required 28 000 gridpoints for the homogeneous model and a much larger number of unknowns for the single prism model to approach the target accuracy of 1 per cent. Only solutions involving second order elements yielded acceptable solutions for the layered block model (Fig. 7c). Unfortunately, even the coarsest second order mesh includes already $\approx$100 000 gridpoints. Further coarsening by reducing the number of elements would have resulted in discretization errors above the 1 per cent line of acceptance.

Enhanced solutions could be obtained, when the mixed-boundary conditions are replaced by infinite elements. The target accuracy could be reached with only 17 000 gridpoints for the homogeneous model (Fig. 7d) and with 29 000 points for the single prism model (Fig. 7e). As for the standard FEM, the first order element solutions performed unsatisfactorily for the layered block model (Fig. 7f), and the computationally more expensive second order elements had to be used for achieving the accuracy required.

Substantial improvements were observed, when the FM-BEM numerical singularity removal was applied. For the homogeneous case (Fig. 7g), the errors were almost zero, but it should be noted that this represents only the accuracy of the singular potential computed with the FM-BEM method (the right-hand side of eq. 7 is zero for homogeneous models). Numerical singularity removal led to marked improvements for the single prism and layered block models. Only 8 900 and 16 500 gridpoints, respectively, were required to achieve the target accuracy (Figs 7h and i). As expected, combined application of infinite elements and numerical singularity removal led to further slight improvements of the results (Figs 7j–l).

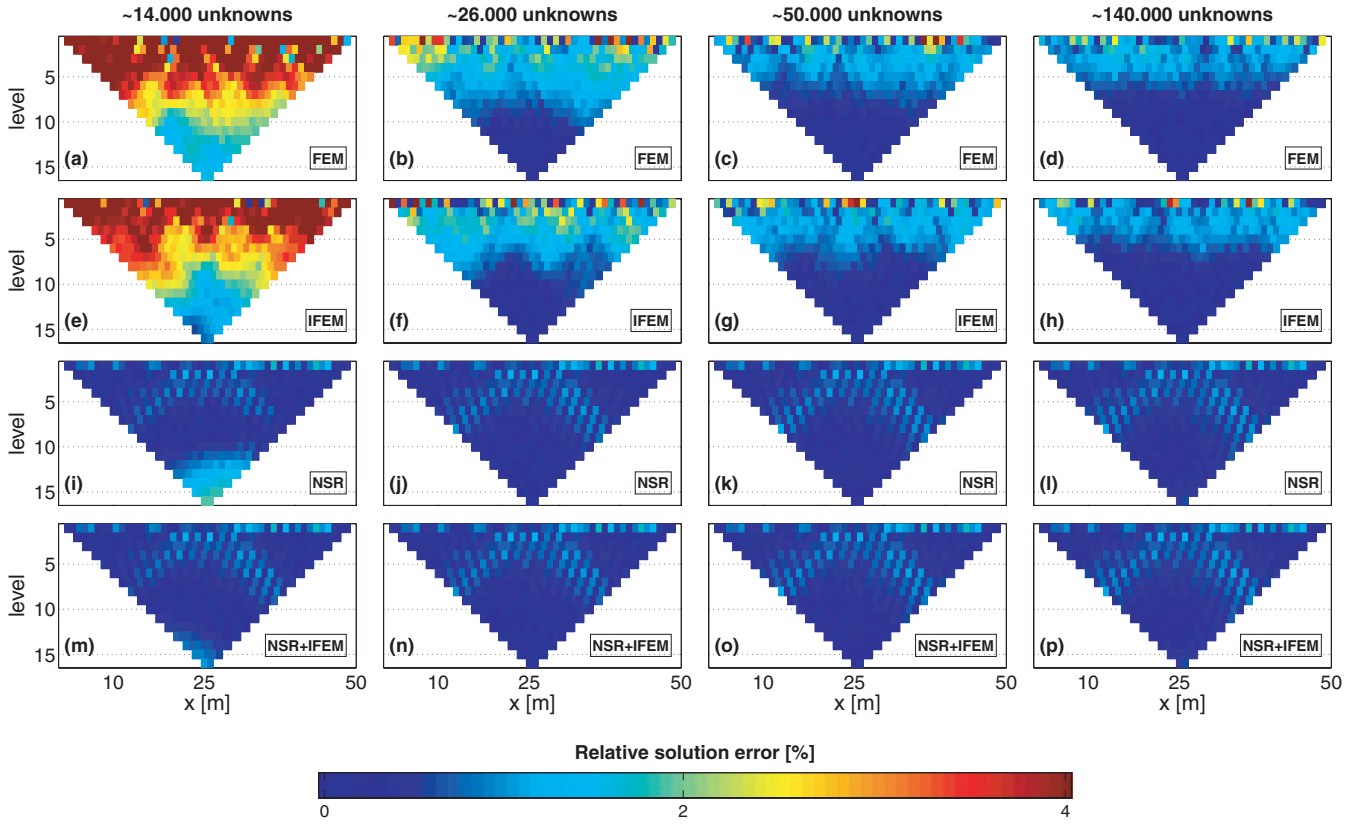

Figure 8. Synthetic Wenner electrode data calculated for the layered block conductivity model with our new forward solver techniques applied. Each subplot shows the relative solution error (in per cent) displayed in the form of the Wenner pseudo-sections. Results are shown for four different mesh sizes (column-wise) and our new forward solver techniques applied (row-wise). Labels: FEM: *SD* FEM calculations, IFEM: *SD* FEM with infinite elements, NSR: Numerical singularity removal.

5.3 Pseudo-sections

Electrical potentials computed along the surface are particularly important, because they are required for predicting measurements with surface electrodes. Therefore, we inspect the accuracy of these potentials in more detail. For that purpose we construct Wenner pseudo-sections by superposing the pole–pole type simulation results discussed in the previous subsection. From the resulting apparent resistivities we subtract the corresponding values from the reference solutions and compute relative errors. Only first order finite elements are considered.

Fig. 8 shows the relative error pseudo-sections for the different computational methods and some selected mesh sizes. Only the results for the most challenging layered block model are displayed. For the conventional FEM calculations (Figs 8a–d), large relative errors occur especially in the first 5 levels of the pseudo-section. As the first levels correspond to short source–receiver distances, these errors are most-likely related to the singularities in the potential solutions. Although a local mesh refinement close to all source electrodes has been applied, the mesh density is apparently still too coarse for approximating the electrical potentials with sufficient accuracy. As expected, the errors decrease for larger meshes (see also Fig. 7).

Similar error distributions are obtained for the calculations involving infinite elements (Figs 8e–h), though the errors are slightly smaller for the calculations on the smallest and the medium sized meshes (Figs 8e and f).

When the singularity removal is applied (Figs 8i–l), the overall error decreases noticeably, such that the calculation with 14 000 unknowns (Fig. 8i) may be already sufficiently accurate to be used within an inversion algorithm. Note that for the conventional FEM calculations (with or without infinite elements) the same accuracy level is not even reached with the largest mesh size (140 000 unknowns). Only minor improvements (compared with the numerical singularity removal) are observed, when both infinite elements and numerical singularity removal are applied (Figs 8m–p).

6 CONCLUSIONS

Efficient inversion procedures for the large amount of data produced by modern geoelectrical multi-electrode arrays require appropriate 3-D geoelectrical forward solvers. Finite element techniques are currently the most powerful option. They allow straightforward implementations of arbitrarily complicated topographies, and they enable application of unstructured meshes. The latter is in our view the key element for achieving computational efficiency. It has to be made sure that an optimized meshing algorithm is employed before any other refinements, such as those presented in this contribution, are envisaged. The literature on meshing algorithms is vast and excellent open source algorithms are available.

The computationally most expensive part of any finite element solver includes the solution of a large and sparse system of equations. Recent developments in mathematical research resulted in direct matrix solvers that allow relatively sizeable systems of equations to be solved. Direct matrix solvers are particularly useful, when

equation systems with many right-hand side arguments are involved, which is the case for 3-D geoelectrical inversion problems. Despite substantial improvements in direct matrix solver techniques, computer memory requirements for realistic 3-D problems remain a problematic issue. Therefore, it is important to minimize the number of unknowns within a finite element mesh, while maintaining a high solution accuracy.

Replacing the traditional Dirichlet or mixed boundary conditions with infinite elements is an attractive option to simultaneously improve the solution accuracy and reduce the number of gridpoints in a finite element mesh. Truncating or fixing the electrical potential at the computational boundaries is well known as a significant source of numerical inaccuracies. Infinite elements provide a more physical and thus more accurate alternative by continuing the electrical potentials to infinity. The subsurface volume surrounding an electrode layout does not need to be meshed with finite elements, which additionally results in savings of gridpoints.

Besides the artificial boundary conditions the surface and subsurface areas near the electrodes represent the second major cause of numerical problems. Since the electrical potentials vary rapidly near the current injection points, the finite elements meshes need to be very dense in these areas, which results in a large number of gridpoints. Singularity removal techniques proposed by (Lowry *et al.* 1989) are a powerful option to alleviate the problem, but they require the singular potential to be computed separately. So far, this was achieved by considering analytical solutions, but in the presence of topography this is not possible. We propose application of a fast multipole boundary element method for computing the singular potentials. This technique includes the principal advantages of the traditional boundary element method and overcomes some of their disadvantages, such as their fully populated system matrix. To our knowledge, this is the first application of the fast multipole boundary element method in geophysics, and we believe that this technique may be an attractive option for other numerical modeling problems.

Extensive numerical tests proved the usefulness of infinite elements and numerical singularity removal using the fast multipole boundary element method. Combined application of both techniques allowed the number of gridpoints to be reduced by a factor of $\approx$6–10 compared with standard finite element techniques. This enables application of direct matrix solvers for realistic 3-D geoelectrical inversion problems, which will improve the computational efficiency dramatically. We hope that these new developments will facilitate 3-D inversion problems to be carried out directly in the field in the near future.

ACKNOWLEDGMENTS

This work was partly supported by the ETH grant 0-20191-04. We thank Prof. Schwab ('Seminar of Applied Mathematics') for helpful advice on the boundary element method and Thomas Günther for helpful discussions on meshing and finite element techniques. We would also like to thank Carsten Rücker and Thomas Günther for providing their finite element solver 'DCFem'. Furthermore, we thank the open source community for continuously providing high quality numerical software free of charge. Without their inspiring work, the research presented in this paper would not have been possible. Special thanks go to the 'Libmesh' developers for their great finite element library and to Olaf Schenk from the University of Basel for his fast direct matrix solver implementation 'Pardiso'. Finally, we thank editor Mark Everett and an anonymous reviewer for helpful comments that improved the quality of the paper.

REFERENCES

Astley, R.J., Macaulay, G.J., Coyette, J.P. & Cremers, L., 1998. Three-dimensional wave-envelope elements of variable order for acoustic radiation and scattering. Part I. formulation in the frequency domain, *J. Acoust. Soc. Am.,* **103**(1), 49–63.

Bettes, P., 1987. A simple wave envelope example, *Commun. Appl. Numer. Methods,* **3,** 77–80.

Bing, Z. & Greenhalgh, S.A., 2001. Finite element three-dimensional direct current resistivity modelling: accuracy and efficiency considerations, *Geophys. J. Int.,* **145**(3), 679–688.

Coggon, J.H., 1971. Electromagnetic and electrical modeling by the finite element method, *Geophysics,* **36**(1), 132–155.

Dey, A. & Morrison, H.F., 1979. Resistivity modeling for arbitrarily shaped three-dimensional structures, *Geophysics,* **44**(4), 753–780.

Dieter, K., Paterson, N. & Grant, F., 1969. Ip and resistivity type curves for three-dimensional bodies, *Geophysics,* **34,** 615–632.

Dreyer, D. & Estorff, O. von., 2003, Improved conditioning of infinite elements for exterior acoustics, *Int. J. Numer. Methods Engg,* **58**(6), 933–953.

Frauenfelder, P. & Lage, C., 2002. Concepts—an object-oriented software package for partial differential equations, *Math. Modell. Numer. Anal.,* **36**(5), 937–951.

Greengard, L. & Rokhlin, V., 1987. A fast algorithm for particle simulations, *J. Comput. Phys.,* **73**(2), 325–348.

Griffiths, D. & Turnbull, J., 1985. A multi-electrode array for resistivity surveying, *First Break,* **3,** 16–20.

Hackbusch, W. & Nowak, Z., 1989. On the fast matrix multiplication in the boundary element method by panel-clustering, *Numerische Mathematik,* **54,** 463–491.

Hestenes, E. & Stiefel, M.R., 1952. Method of conjugate gradients for solving linear systems, *J. Res. Nat. Bur. Standarts,* **49,** 409–436.

Hvozdara, M. & Kaikkonen, P., 1998. An integral equations solution of the forward D.C. geoelectric problem for a 3-d body of inhomogeneous conductivity buried in a halfspace, *J. appl. Geophys.,* **39,** 95–107.

Karypis, G. & Kumar, V., 1995. *A Fast and High Quality Multilevel Scheme for Partitioning Irregular Graphs,* in *Proceedings of the 1995 International Conference on Parallel Processing*, Urbana-Champain, Illinois, USA, pp. 113–122.

Kirk, B., Peterson, J., Stogner, R. & Carey, G., 2006. libmesh: a C++ library for parallel adaptive mesh refinement/coarsening simulations, *Engg. Comput.,* **22,** 237–254.

Lage, C., 1995. *Analyse, Entwurf und Implementation von Randelementmethoden*. Unpublished doctoral dissertation, Inst. f. Prakt. Math., Universitaet Kiel.

Lee, T., 1975. An integral equation and its solution for some two and three-dimensional problems in resistivity and induced polarization, *Geophys. J.,* **42,** 81–95.

Li, Y. & Spitzer, K., 2002. Three-dimensional DC resistivity forward modelling using finite elements in comparison with finite-difference solutions, *Geophys. J. Int.,* **151**(3), 924–934.

Loke, M. & Barker, R., 1996. Practical techniques for 3d resistivity surveys and data inversion, *Geophys. Prospect.,* **44**(3), 499–523.

Lowry, T., Allen, M.B. & Shive, P.N., 1989. Singularity removal: a refinement of resistivity modeling techniques, *Geophysics,* **54**(6), 766–774.

Ma, Q., 2002. The boundary element method for 3-d dc resistivity modeling in layered earth, *Geophysics,* **67**(2), 610–617.

Mendonca, C.A., 2003. The face-current concept and its application to survey design in electrical exploration, *Geophysics,* **68**(3), 900–910.

Mufti, I.R., 1976. Finite-difference resistivity modeling for arbitrarily shaped two-dimensional structures, *Geophysics,* **41**(1), 62–78.

Pain, C.C., Herwanger, J.V., Worthington, M.H. & Oliveira, C.R. (ed.) 2002. Effective multidimensional resistivity inversion using finite-element techniques. *Geophys. J. Int.,* **151**(3), 710–728.

Pridmore, D.F., Hohmann, G.W., Ward, S.H. & Sill, W.R., 1981. An investigation of finite-element modeling for electrical and electromagnetic data in three dimensions, *Geophysics,* **46**(7), 1009–1024.

Rücker, C., Günther, T. & Spitzer, K., 2006. Three-dimensional modelling and inversion of dc resistivity data incorporating topography—I. Modelling, *Geophys. J. Int.,* **166,** 495–505.

Sasaki, Y., 1994. 3-D resistivity inversion using the finite-element method, *Geophysics,* **59**(12), 1839–1848.

Sauter, S. & Schwab, C., 2004. *Randelementmethoden*. Teubner.

Schenk, O., Gartner, K., Fichtner, W. & Stricker, A., 2001. Pardiso: a high-performance serial and parallel sparse linear solver in semiconductor device simulation, *Future Generat. Comput. Syst.,* **18**(1), 69–78.

Schenk, O., Röllin, S. & Hagemann, M., 2003. *Recent Advances in Sparse Linear Solver Technology for Semiconductor Device Simulation Matrices,* in *Proceedings of the 2003 International Conference on Simulation of Semiconductor Processes and Devices,* pp. 103–108.

Shewchuk, J.R., 1996. Triangle: engineering a 2D quality mesh generator and delaunay triangulator, in *Applied Computational Geometry: Towards Geometric Engineering*,Vol. 1148, pp. 203–222, eds Lin, M.C. & Manocha, D., Springer-Verlag, Berlin (From the First ACM Workshop on Applied Computational Geometry.)

Si, H. & Gaertner, K., 2005. Meshing piecewise linear complexes by constrained delaunay tetrahedralization. *Proceedings of the 14th International Meshing Roundtable*, San Diego, CA, pp. 147–163.

Spitzer, K., 1995. A 3-d finite-difference algorithm for dc resistivity modeling using conjugate-gradient methods. *Geophys. J. Int.,* **123**(3), 903–914.

Stummer, P., Maurer, H., Horstmeyer, H. & Green, A., 2002. Optimization of dc resistivity data acquisition: real-time experimental design and a new multielectrode system. *Geosci. Remote Sens., IEEE Trans.,* **40**(12), 2727–2735.

Wang, T., Fang, S. & Mezzatesta, A., 2000. Three-dimensional finite-difference resistivity modeling using an upgridding method. *Geosci. Remote Sens., IEEE Trans.,* **38**(4), 1544–1550.

Xu, S.-Z., Zhao, S. & Ni, Y., 1998. A boundary element method for 2-d dc resistivity modeling with a point current source. *Geophysics,* **63**(2), 399–404.

Zhao, S. & Yedlin, M.J., 1996. Some refinements on the finite-difference method for 3-d dc resistivity modeling. *Geophysics,* **61**(5), 1301–1307.

Zienkiewicz., 1977. *The Finite Element Method*, McGraw Hill, London.

APPENDIX A: PANEL CLUSTERING METHOD

As described in Section 4.1, the boundary integral equation employed for calculating the singular potentials leads to a linear system of equations $\mathbf{A}\mathbf{u}_{\mathrm{h}}^{\mathrm{s}} = \mathbf{B}\mathbf{q}$ with the element integrals

$$\mathbf{A}_{ij} = 1/2 \int_{\Gamma_s} \phi_i(\mathbf{r})\phi_j(\mathbf{r}')\,\mathrm{d}S_{\mathbf{r}'} + \int_{\Gamma_s}\int_{\Gamma_s} \phi_i(\mathbf{r})\frac{\partial G(\mathbf{r},\mathbf{r}')}{\partial \mathbf{n}}\phi_j(\mathbf{r}')\,\mathrm{d}S_{\mathbf{r}}\,\mathrm{d}S_{\mathbf{r}'} \tag{A1a}$$

$$\mathbf{B}_{ij} = \int_{\Gamma_s}\int_{\Gamma_s} \phi_i(\mathbf{r})G(\mathbf{r},\mathbf{r}')\phi_j(\mathbf{r}')\,\mathrm{d}S_{\mathbf{r}}\,\mathrm{d}S_{\mathbf{r}'}. \tag{A1b}$$

The Green's function, respectively, its normal derivative in the double integrals in eqs (A1a) and (A1b) couple each degree of freedom on the surface mesh located at node i (position $\mathbf{r}$) to all other degrees of freedoms at nodes j (positions $\mathbf{r}'$) and thereby lead to fully populated matrices $\mathbf{A}$ and $\mathbf{B}$. This is in contrast to finite element formulations for which only locally defined shape functions, respectively, their gradients appear in the element integrals and hence very sparse system matrices result. As a consequence, the computational costs, memory consumption and solution time, for conventional BEM formulations exhibit an unfavorable scaling behavior proportional to $\sim \mathcal{O}(N^2)$ where N is the number of unknowns. In the 'Panel Clustering Method', whose basic principles are explained in the following, an approximation of the Green's function and its normal derivative is employed to account for this major drawback.

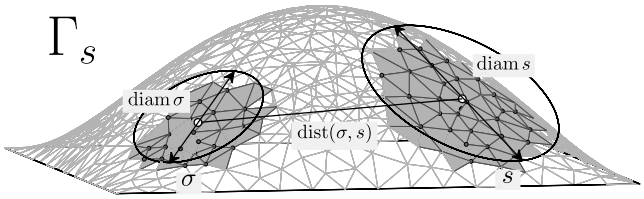

Figure A1. Example of two cluster σ and s on a typical 3-D surface mesh used for the BEM. diam (s) or diam (σ) denote the cluster diameters and $dist(x, y)$ denotes the distance of two clusters towards each other.

A1 Green's function approximation on cluster-pairs

The Green's function that is needed when solving the 3-D Poisson equation for the singular potentials takes the form

$$G(\mathbf{r},\mathbf{r}') = \frac{1}{4\pi\sigma_0\,|\mathbf{r}-\mathbf{r}'|}. \tag{A2}$$

It varies rapidly for short $\mathbf{r}$ to $\mathbf{r}'$ distances but shows only slight variations for larger $\mathbf{r}$ to $\mathbf{r}'$ distances. Therefore, it is beneficial to distinguish between a nearfield, where the double integrals in eqs (A1a) and (A1b) are evaluated exactly and a farfield where these integrals are approximated. The farfield-approximation employed in the panel clustering method relies on the idea of 'multipole moments' originally developed by (Greengard & Rokhlin 1987). Fig. A2 depicts a sketch of the underlying basic idea. In the conventional BEM for each Green's function source point $\mathbf{r}$ the coupling to all other Green's function points $\mathbf{r}'$ are evaluated exactly when calculating the double integrals which yields numerical costs of the order $\sim \mathcal{O}(N^2)$ (Fig. A2a). In the panel clustering method Green's function evaluation points are grouped in the farfield into clusters such that the combined effect of all Green's function points $\mathbf{r}'$ belonging to one cluster are subsumed into multipole moments. Subsequently only the coupling of the Green's function source point $\mathbf{r}$ to the multipole moment needs to be evaluated (Fig. A2b). The same approximation can be applied locally around the Green's function source points to yield an algorithm with numerical costs that scale as $\sim \mathcal{O}[N \log^{\alpha}(N)]$ (Fig. A2c). This scheme requires an approximation of the Green's function on cluster pairs (s, σ) where the variables $\mathbf{r}$ and $\mathbf{r}'$ are separated:

$$G(\mathbf{r},\mathbf{r}') \approx \tilde{G}(\mathbf{r},\mathbf{r}') = \sum_{(\vec{\mu},\vec{\nu})} \mathbf{K}_{\vec{\mu},\vec{\nu}}\,\Phi_{\sigma}(\mathbf{r})\Psi_{s}(\mathbf{r}'). \tag{A3}$$

Here $\mathbf{K}_{\vec{\mu},\vec{\nu}}$ is a $k \times k$-matrix of expansion coefficients defined for the cluster pair (s, σ). Φ_{σ} and Ψ_{s} are the expansion functions defined on cluster s, respectively, cluster σ. Different Green's function expansions can be employed, for example, an expansion into the three spatial coordinates by Taylor series, or, as is used within this work, a multipole expansion based on spherical harmonics (see Sauter & Schwab 2004, for more details).

Whether a pair of basis functions belongs to the farfield or to the nearfield and hence the degree to which the BEM system matrices are approximated is controlled by a parameter η:

$$\eta\,\mathrm{dist}(\sigma, s) \geq \max(\mathrm{diam}\,\sigma, \mathrm{diam}\,s). \tag{A4}$$

Here diam σ and diam s are the diameters of the two clusters and dist (σ, s) is their distance towards each other. For each possible cluster pair (s, σ) a Green's function approximation according to eq. (A3)

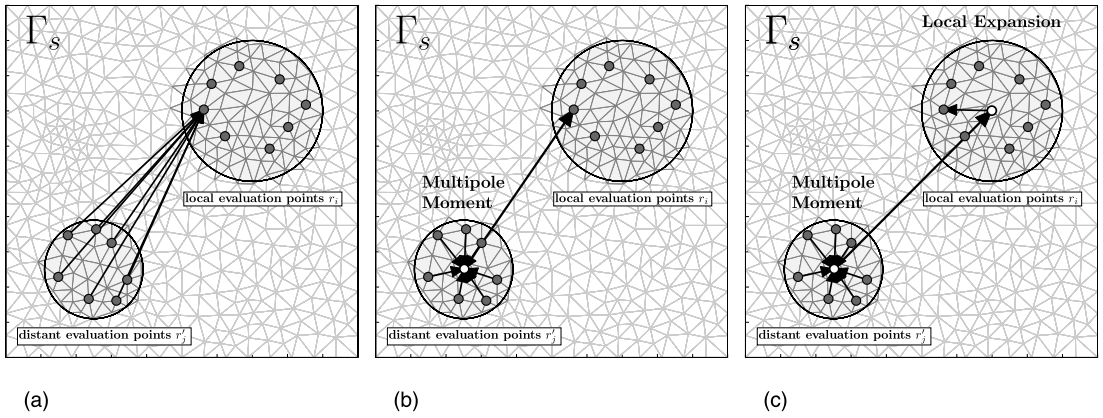

Figure A2. Sketch of the basic idea of the multipole method. Three different approaches of evaluating the Green's function $G(\mathbf{r}, \mathbf{r}')$ for a set of evaluation points $\mathbf{r}_i$ and $\mathbf{r}'_j$ on a BEM surface mesh are shown. (a) leads to an algorithm with computational costs $\sim \mathcal{O}(N^2)$ whereas (c) results into an algorithm whose computational costs scale as $\sim \mathcal{O}(N)$.

is employed if eq. (A4) is valid, otherwise all pairs of basis functions (ϕ_i, ϕ_j) with $\phi_i \in \sigma$ and $\phi_j \in s$ are part of the nearfield, that is, the corresponding matrix entries $\mathbf{A}_{ij}$ are calculated exactly. The scheme by which potential cluster pairs are constructed is outlined in Section A3. By choosing η carefully the error introduced due to the panel-clustering method can be limited to a range which is in the order or smaller than the discretization error due to the surface triangulation. Within this work we use $\eta = 0.5$.

A2 Matrix representation and matrix vector multiplication

The Green's function approximation (eq. A3) does not only reduce the computational costs, but also allows the system matrices **A** and **B** to be approximated. This results in a significant reduction of the overall memory requirements. In the following we denote all nodes belonging to cluster s with I_s and similarly all nodes belonging to cluster σ with I_σ. While the matrix entries for all elements belonging to the nearfield are calculated exactly, all matrix entries A_{ij} for $i \in I_s$ and $j \in I_\sigma$ can be approximated by a product of three matrices $\mathbf{L}^\sigma$, $\mathbf{K}$ and $(\mathbf{R}^s)^\top$:

$$\begin{aligned}\mathbf{A}_{ij} \approx \tilde{\mathbf{A}}_{ij} &:= \int_\Gamma \int_\Gamma \phi_i(\mathbf{r})\, \tilde{G}(\mathbf{r}, \mathbf{r}')\, \phi_j(\mathbf{r}')\, \mathrm{d}S_{\mathbf{r}} \mathrm{d}S'_{\mathbf{r}} \\ &= \sum_{(\vec{\mu},\vec{\nu})} \mathbf{L}^\sigma_{i,\vec{\nu}} \mathbf{K}_{\vec{\nu},\vec{\mu}} \mathbf{R}^s_{j,\vec{\mu}} = \left[\mathbf{L}^\sigma \cdot \mathbf{K} \cdot (\mathbf{R}^s)^\top\right]_{ij} \end{aligned} \tag{A5}$$

with

$$\mathbf{L}^\sigma_{i,\vec{\nu}} := \int_\Gamma \phi_i(\mathbf{r})\, \Psi_s(\mathbf{r}')\, \mathrm{d}S_{\mathbf{r}'}, \; \mathbf{R}^s_{j,\vec{\mu}} := \int_\Gamma \phi_j(\mathbf{r})\, \Phi_\sigma(\mathbf{r}')\, \mathrm{d}S_{\mathbf{r}}.$$

For simplicity the approximation is demonstrated here only for matrix **A**. Fig. A3 shows a sketch of the structure of $\tilde{\mathbf{A}}$: The exact nearfield matrix entries close to the diagonal of $\tilde{\mathbf{A}}$ are highlighted together with one matrix block that is approximated by a Green's function expansion on a pair of clusters. Note that the nodes indices I_σ and I_s for a cluster pair (σ, s) are in general distributed across the matrix but for simplicity they are shown in the form of a rectangular block. Each of the approximated matrix blocks consists of a multiplication of three matrices as in eq. (A5). If we denote the number of nodes in the clusters s and σ by N_s, respectively N_σ, then the three matrices have the dimensions $N_\sigma \times k$, $k \times k$ and $k \times N_s$, as shown in Fig. A3. Here k denotes the number of expansion coefficients, which is significantly smaller than N_σ and N_s.

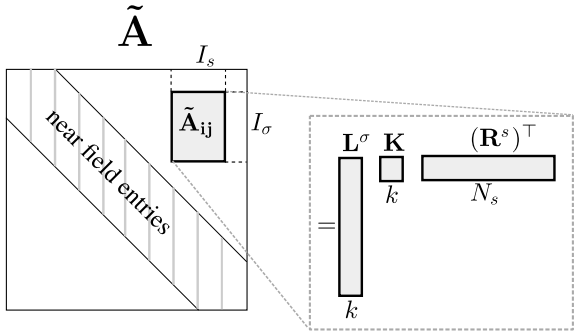

Figure A3. Sketch of the structure of the approximated system matrix $\tilde{\mathbf{A}}$. For all pairs of basis functions (ϕ_i, ϕ_j) in the farfield, exact nearfield entries result into $\tilde{\mathbf{A}}$ whereas for all pairs of basis functions that are in the farfield an approximation is performed on pairs of clusters. For each cluster pair the corresponding matrix entries $\tilde{\mathbf{A}}_{ij}$ are given by a product of three matrices $\mathbf{L}^\sigma$, $\mathbf{K}$ and $\mathbf{R}^s$.

The system matrices **A** and **B** are not given explicitly in the panel-clustering method but are defined in terms of the approximation scheme as outlined above. When solving the BEM equations with iterative matrix solvers, only matrix vector products are needed. The panel-clustering method provides a fast way of evaluating these products. The computational savings become obvious if we look at the matrix-vector multiplication of the matrix block $\tilde{\mathbf{A}}_{ij}$ with a vector **u**:

$$(\tilde{\mathbf{A}}\mathbf{u})_i = \sum_{j \in I_s} \tilde{\mathbf{A}}_{ij} \mathbf{u}_j = \sum_{\vec{\nu}} \mathbf{L}^\sigma_{i,\vec{\nu}} \sum_{\vec{\mu}} \mathbf{K}^b_{\vec{\nu},\vec{\mu}} \sum_{j \in I_s} \mathbf{u}_j \mathbf{R}^s_{j,\vec{\mu}}, \tag{A6}$$

Clearly this product needs considerably less floating point operations than a full matrix vector multiplication with the matrix block $\mathbf{A}_{ij}$.

A3 Multilevel scheme

In the previous sections the Green's function approximation on a single cluster pair was described and it was outlined that such an approximation results in a significant improvement on the performance of the BEM. The question remains, how the set of cluster pairs can be constructed in an optimal fashion. The panel-clustering method employs a multilevel scheme in which a hierarchic tree structure of clusters $\mathcal{T}$ is generated.

The root of the cluster tree $\mathcal{T}$ is constructed by a minimal axis-parallel cuboid that encloses the entire surface mesh Γ_s. The root of $\mathcal{T}$ consists of all basis functions or nodes in Γ_s. Subsequently the cuboid is subdivided in eight congruent cuboids. The nodes of the surface mesh that are contained in these cuboids form the eight children of the root of $\mathcal{T}$. This subdivision is repeated recursively for all children until the smallest cluster consists of a predefined minimum number of nodes.

The resulting cluster tree $\mathcal{T}$ is used to construct a set of cluster pairs P^{far} for which the Greens function approximation (eq. A3) is applied, and a set of cluster pairs P^{near} for which exact evaluations are used. Eq. (A4) is used to decide whether a cluster pair belongs to P^{near} or P^{far}.

The process starts with a cluster pair (σ, s) where σ and s are both the root of $\mathcal{T}$, that is, both contain all nodes of Γ_s. If eq. (A4) is true for (σ, s), which is obviously not the case for the root clusters, then (σ, s) belongs to P^{far}, otherwise the process is continued recursively for the children cluster pairs. Thereby, the children cluster pairs of (σ, s) are all combinations (σ', s'), where σ' is one of the children of σ in $\mathcal{T}$ and correspondingly s' is one of the children of s in $\mathcal{T}$. Cluster pairs (σ, s), for which eq. (A4) is not true, will only be appended to P^{near} if they have no children, that is, if both clusters σ and s are not further subdivided in $\mathcal{T}$.

Finally each pair of basis functions (ϕ_i, ϕ_j) [corresponding to a pair of surface mesh nodes (i, j)] belongs either to the farfield P^{far} or to the nearfield P^{near}. For all $(\phi_i, \phi_j) \in P^{\text{near}}$ exact calculations are performed resulting into nearfield entries $\mathbf{A}_{ij}$ as sketched in Fig. A3 whereas for all pairs of basis functions $(\phi_i, \phi_j) \in P^{\text{far}}$ approximations on cluster pairs as performed as outlined above. Since the expansion functions Φ_σ, Ψ_s in any cluster pair (σ, s) can be written as a combination of functions on the cells, all operations are performed on triangles and then 'raised' to higher levels in the cluster tree. Altogether, the panel-clustering method results into a boundary element implementation for which the computational costs scale as $\sim \mathcal{O}[N \log^5(N)]$ instead of the $\sim \mathcal{O}(N^2)$ scaling for conventional BEM implementations.

For the singularity removal technique described in Section 2.2 the singular potentials may be required not only along the surface Γ_s, but also inside the volume at all nodes of the finite element mesh. Once the surface solution is found with the panel-clustering method, the same technique can be employed for evaluating the volume solution values. For this purpose, an additional cluster tree $\mathcal{T}_{\text{vol}}$ is constructed for the finite element mesh and the clustering algorithm described above is applied to pairs of clusters (σ, s) with $\sigma \in \mathcal{T}$ and $s \in \mathcal{T}_{\text{vol}}$.